Article

Cell Reports

An Intrinsically Disordered Peptide from Ebola Virus VP35 Controls Viral RNA Synthesis by Modulating Nucleoprotein-RNA Interactions

Graphical Abstract

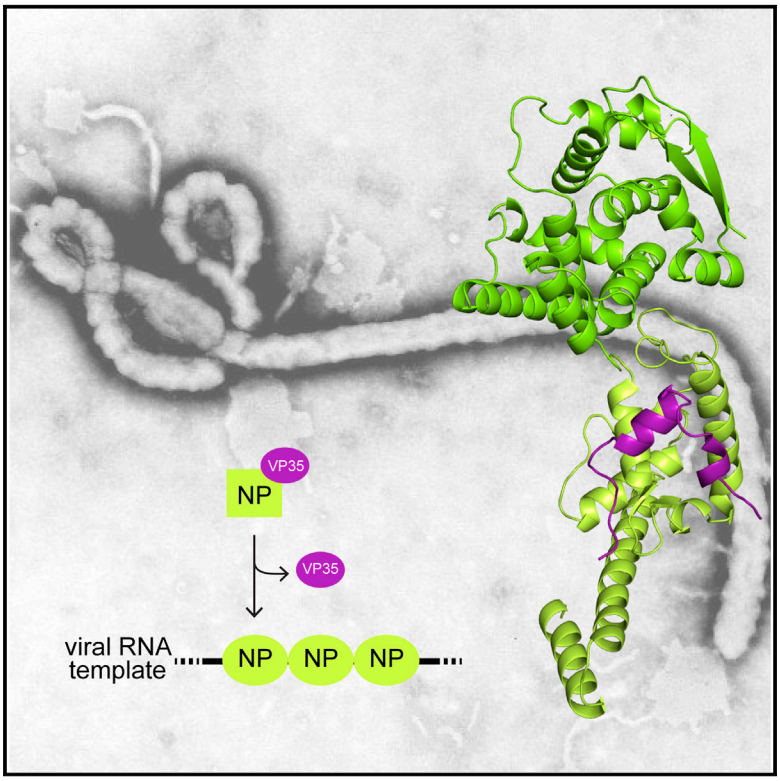

Authors

Daisy W. Leung, Dominika Borek, ..., Christopher F. Basler, Gaya K. Amarasinghe

Correspondence

gamarasinghe@path.wustl.edu

In Brief

Ebola virus RNA synthesis is a tightly controlled process. Leung et al. reveal how a peptide derived from Ebola VP35 protein impacts viral RNA synthesis by modulating interactions between Ebola virus nucleoprotein and RNA.

Highlights

- The minimum Ebola virus VP35 peptide that binds nucleoprotein is defined
- The structure of the VP35 peptide/N-terminal nucleoprotein complex is determined
- A role for VP35 peptide in viral RNA synthesis is defined
- A possible framework to target the VP35/nucleoprotein interface is defined

Accession Numbers

4YPI

Leung et al., 2015, Cell Reports *11*, 376–389
April 21, 2015
http://dx.doi.org/10.1016/j.celrep.2015.03.034

CellPress

OPEN ACCESS
CellPress

Cell Reports
Article

An Intrinsically Disordered Peptide from Ebola Virus VP35 Controls Viral RNA Synthesis by Modulating Nucleoprotein-RNA Interactions

Daisy W. Leung,[1,7] Dominika Borek,[2,7] Priya Luthra,[3] Jennifer M. Binning,[1] Manu Anantpadma,[4] Gai Liu,[1] Ian B. Harvey,[1] Zhaoming Su,[5] Ariel Endlich-Frazier,[3] Juanli Pan,[1] Reed S. Shabman,[3,6] Wah Chiu,[5] Robert A. Davey,[4] Zbyszek Otwinowski,[2] Christopher F. Basler,[3] and Gaya K. Amarasinghe[1,*]

[1]Department of Pathology and Immunology, Washington University School of Medicine, St Louis, MO 63110, USA
[2]Departments of Biophysics and Biochemistry and Center for Structural Genomics of Infectious Diseases, University of Texas Southwestern Medical Center at Dallas, Dallas, TX 75390, USA
[3]Department of Microbiology, Icahn School of Medicine at Mount Sinai, New York, NY 10029, USA
[4]Department of Virology and Immunology, Texas Biomedical Research Institute, San Antonio, TX 78227, USA
[5]National Center for Macromolecular Imaging, Verna and Marrs McLean Department of Biochemistry and Molecular Biology, Baylor College of Medicine, Houston, TX 77030, USA
[6]Present address: Virology Group, J. Craig Venter Institute, Rockville, MD 20850, USA
[7]Co-first author
*Correspondence: gamarasinghe@path.wustl.edu
http://dx.doi.org/10.1016/j.celrep.2015.03.034

SUMMARY

During viral RNA synthesis, Ebola virus (EBOV) nucleoprotein (NP) alternates between an RNA-template-bound form and a template-free form to provide the viral polymerase access to the RNA template. In addition, newly synthesized NP must be prevented from indiscriminately binding to noncognate RNAs. Here, we investigate the molecular bases for these critical processes. We identify an intrinsically disordered peptide derived from EBOV VP35 (NPBP, residues 20–48) that binds NP with high affinity and specificity, inhibits NP oligomerization, and releases RNA from NP-RNA complexes in vitro. The structure of the NPBP/ΔNP_{NTD} complex, solved to 3.7 Å resolution, reveals how NPBP peptide occludes a large surface area that is important for NP-NP and NP-RNA interactions and for viral RNA synthesis. Together, our results identify a highly conserved viral interface that is important for EBOV replication and can be targeted for therapeutic development.

INTRODUCTION

Ebolaviruses and marburgviruses are nonsegmented negative-sense RNA viruses (NNSVs) that cause severe hemorrhagic fever (Sanchez et al., 2006). Because of the severity of filovirus disease, which is associated with case fatality rates approaching 90% during some outbreaks, ebolaviruses and marburgviruses remain significant threats to global human health. The recent epidemic in Western Africa caused by Ebola virus (EBOV) Makona variant is the largest filovirus outbreak on record, and the subsequent import of EBOV to non-African countries highlights the public health impact of these zoonotic pathogens.

Like other non-segmented negative-strand virus (NNSV) family members, EBOV has a single-stranded RNA (ssRNA) genome that undergoes transcription upon entry into the host cytosol prior to the generation of viral proteins (Mühlberger, 2007; Sanchez et al., 2006). The roughly 19-kb ebolavirus genome has seven genes that encode for at least eight distinct translation products (Sanchez and Kiley, 1987; Sanchez et al., 1993, 2007; Shabman et al., 2014). Viral genome replication and transcription of individual genes into distinct 5′-capped, 3′-polyadenylated monocistronic mRNAs are carried out by the viral RNA-dependent RNA polymerase complex (RdRp) (Mühlberger, 2007). This complex consists of the enzymatic component of the RDRP, the large protein (L), along with the viral nucleoprotein (NP), viral protein (VP)35 and VP30, and acts upon the nucleocapsid, which consists of single-stranded viral genomic or antigenomic RNAs (Mühlberger, 2007) that are encapsidated by NP. The EBOV core nucleocapsid protects ssRNAs from degradation, similar to that observed for paramyxoviruses and rhabdoviruses (Masters and Banerjee, 1988).

Based on sequence homology, the filovirus NP has a paramyxovirus/filovirus conserved region spanning residues 1 to 450 and a region unique to filoviruses from 451 to 739 (Shi et al., 2008; Watanabe et al., 2006) (Figures 1A and S1A). The N-terminal region mediates NP self-association and forms helical tube-like structures in vitro (Watanabe et al., 2006) and in cells (Huang et al., 2002). Mapping studies indicate that the NP C terminus contributes to NP-VP40 interaction and NP incorporation into ebolavirus-like particles (Noda et al., 2007). Recently, a crystal structure of the EBOV NP C-terminal residues encompassing 641–739 was described (Dziubańska et al., 2014), but how this structure contributes to EBOV infection is unknown.

Viral polymerase cofactor VP35 is a suppressor of innate immune signaling and is also critical for viral RNA synthesis (Feng

et al., 2007; Luthra et al., 2013; Prins et al., 2009; Schümann et al., 2009). Its role in RNA synthesis is thought to be functionally analogous to the P protein in other NNSVs (Sanchez et al., 2006). VP35 has an N-terminal oligomerization domain and a C-terminal interferon inhibitory domain (IID), which binds double-stranded RNA (dsRNA) and is critical for innate immune inhibition (Basler et al., 2003; Hartman et al., 2004; Leung et al., 2009, 2010b). The N-terminal oligomerization domain is thought to participate in protein-protein interactions, including VP35 self-association (Möller et al., 2005; Reid et al., 2005) as well as association with the viral polymerase L (Trunschke et al., 2013). VP35 oligomerization is also important for RNA synthesis (Möller et al., 2005), but it appears to be dispensable for VP35/NP co-localization (Möller et al., 2005).

Despite previous efforts, it is unclear how VP35-NP interactions modulate EBOV RNA synthesis. Here, we describe an interaction between the EBOV VP35 and NP proteins that critically impacts NP function and EBOV RNA synthesis.

RESULTS

The N Terminus of NP Is Important for Oligomerization

Previous deletion analysis of EBOV NP revealed that three truncations (residues 2–150, 151–300, and 301–450) resulted in loss of NP function in the viral RDRP complex (Watanabe et al., 2006). In order to identify specific residues involved in NP-NP association, we generated a series of truncation constructs (Figure S1A), which were evaluated in both low- (150 mM NaCl) and high-salt (500 mM NaCl) buffers. All constructs tested, including NP 1–457 and 25–457, formed large homo-oligomeric complexes as NP elutes in the void volume in buffer containing 150 mM NaCl (Figure 1B). In buffer with 500 mM NaCl, many constructs displayed behavior similar to those in 150 mM NaCl except for NP 25–457 (ΔNP_{NTD}), where some protein eluted in the included volume and some near the void volume (V_0), representing a multimeric population that is likely an aggregate (Figure 1C). Moreover, we observed >60% monodispersed (well-behaved) ΔNP_{NTD} protein in solution at concentrations >10 mg/ml based on multiangle light scattering (MALS) studies. Results from finer truncations (i.e., two- to three-residue deletions) within the first 24 residues suggested a critical role for residues 21–22 as proteins starting at residue 23 eluted in the included volume. In order to further evaluate the impact of Y21 and H22, we generated single mutants (Y21A or H22A) and a double mutant (Y21A/H22A) of NP 1–457. Of these NP mutants, only the Y21A/H22A double mutant eluted in the included volume and the peak displayed low levels of polydispersity (Figure 1D). These results further support an important role for the NP paramyxovirus/filovirus conserved region (NP residues 1–457) in NP-NP self-association.

The N and C Termini of NP Are Required for Viral RNA Synthesis

In order to further test the role of NP-NP self-association in viral RNA synthesis, we tested N- and C-terminal truncations of NP using a minigenome (MG) assay that uses a model Ebola virus genomic RNA encoding *Renilla* luciferase as a template for transcription and replication by a viral polymerase complex reconstituted by expression of NP, VP35, VP30, and L (Mühlberger, 2007; Mühlberger et al., 1999). In these assays, mutation of Y21A/H22A in the context of the full-length NP and the 20–739 NP construct resulted in a complete loss of function (Figures 1E and S1B). Deletion of the first 19 residues of NP (NP 20–739) results in a partial loss in activity (~60%), suggesting that these residues are important, but not essential, for activity. In contrast, C-terminal deletion mutants, such as NP 1–550 or NP 1–601, were severely impaired (<10% of wild-type [WT] activity) in the MG assay (Figure 1E).

We tested three additional EBOV NP constructs, NP 25–739, NP 25–550, and NP 1–550, for their ability to support MG activity in the presence and absence of WT NP (Figures 1F and S1C). Expression of N-terminal NP truncations, such as NP 25–739 and NP 25–550, did not affect the MG function of NP. However, a C-terminal truncation construct that retained the entire N terminus (NP 1–550) and the ability to oligomerize displayed dominant-negative activity, suggesting that interactions through the N terminus limit the MG activity of the WT NP (1–739). Collectively these results support a role of both the NP N and C termini during viral RNA synthesis.

NPBP Peptide from VP35 Is Necessary and Sufficient to Bind NP

EBOV NP associates with EBOV VP35 in the context of the replication complex, and this interaction is thought to play a major role during viral RNA synthesis (Elliott et al., 1993; Huang et al., 2002). Previous analyses of EBOV VP35 identified several regions that are highly conserved among filoviruses, including an N-terminal oligomerization domain and a C-terminal IID (Figure 2A) (Hartman et al., 2004; Leung et al., 2010a; Reid et al., 2005). However, sequence analysis of *ebolavirus* VP35s revealed an additional, highly conserved region N-terminal to the previously predicted oligomerization domain (Figure S1D) (Reid et al., 2005). To determine whether this region in VP35 is required to support viral RNA synthesis, we generated a series of VP35 truncated constructs, where we systematically deleted ten-residue segments from the N terminus and evaluated the role of these residues in viral RNA synthesis using the MG assay. The resulting data revealed that the first 19 residues are largely dispensable for MG activity (Figure 2B). In contrast, residues 20–52 are critical for EBOV MG activity, as N-terminal truncations that extend into this conserved region, including truncations such as in the 30–340 construct, resulted in >60% loss of activity relative to WT VP35 (residues 1-340). Deletion of the entire NPBP region plus the first 19 amino acids results in near-complete loss of MG activity, suggesting that the entire NPBP is required for activity.

In order to determine the molecular basis for this observation, we next tested interactions between VP35 and NP using in vitro binding assays and various VP35 and NP truncations. These results revealed that EBOV ΔNP_{NTD} was sufficient for high-affinity binding to the EBOV VP35 N terminus. These studies also revealed that VP35-NP association is coordinated, at least in part, through the VP35 N terminus, as VP35 1–168 binds NP whereas VP35 58–340 does not (Figures 2C and S2A). In order to further characterize this interaction, we generated a series of peptides spanning VP35 residues 20–52.

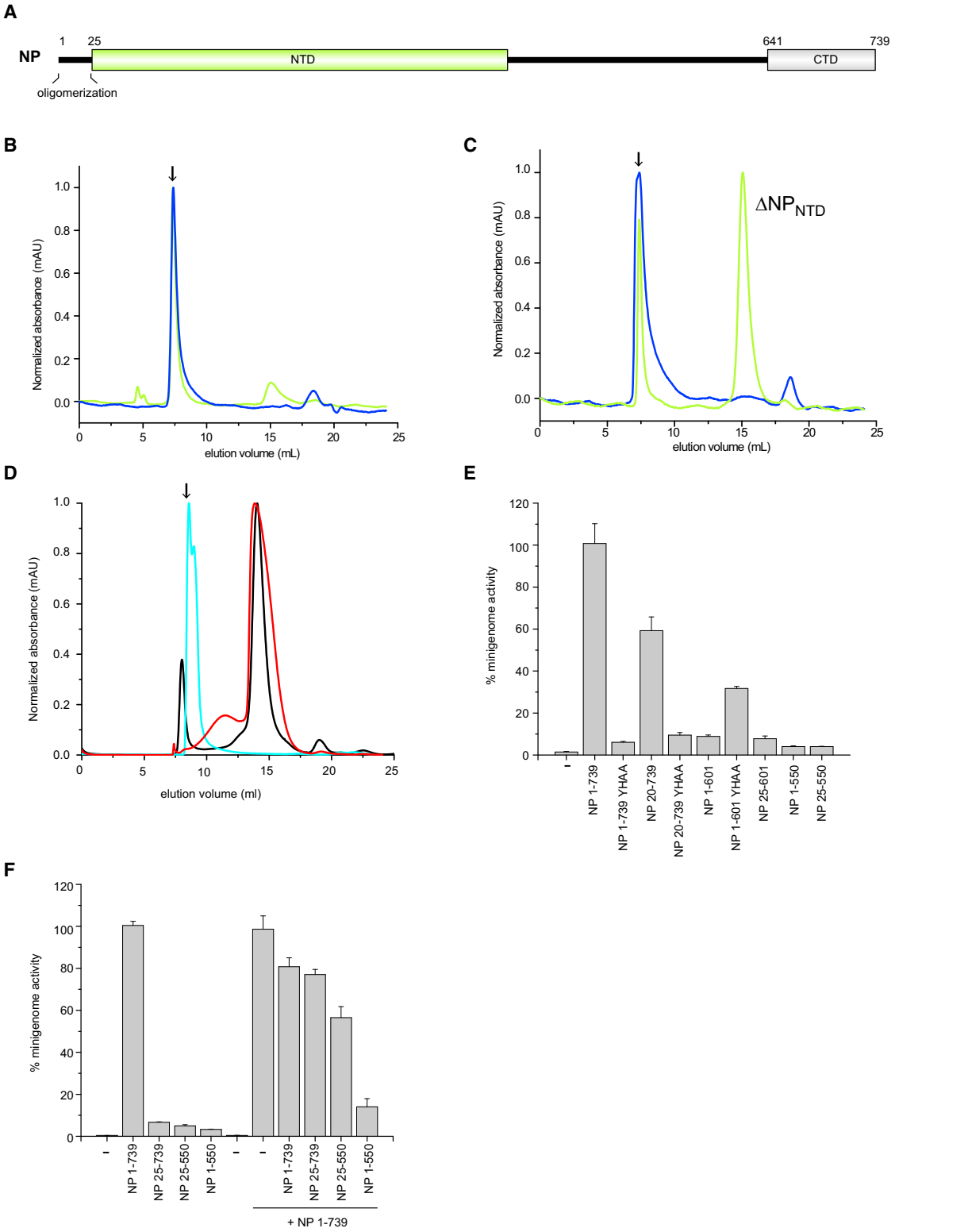

Figure 1. The First 24 Residues of the EBOV NP Are Important for Oligomerization and Replication

(A) Domain organization of EBOV NP protein, including regions identified in this study.

(B and C) Size-exclusion chromatography results for NP_{NTD} (residues 1–457, blue) and ΔNP_{NTD} (residues 25–457, green) in (B) 150 mM NaCl and (C) 500 mM NaCl buffer.

(legend continued on next page)

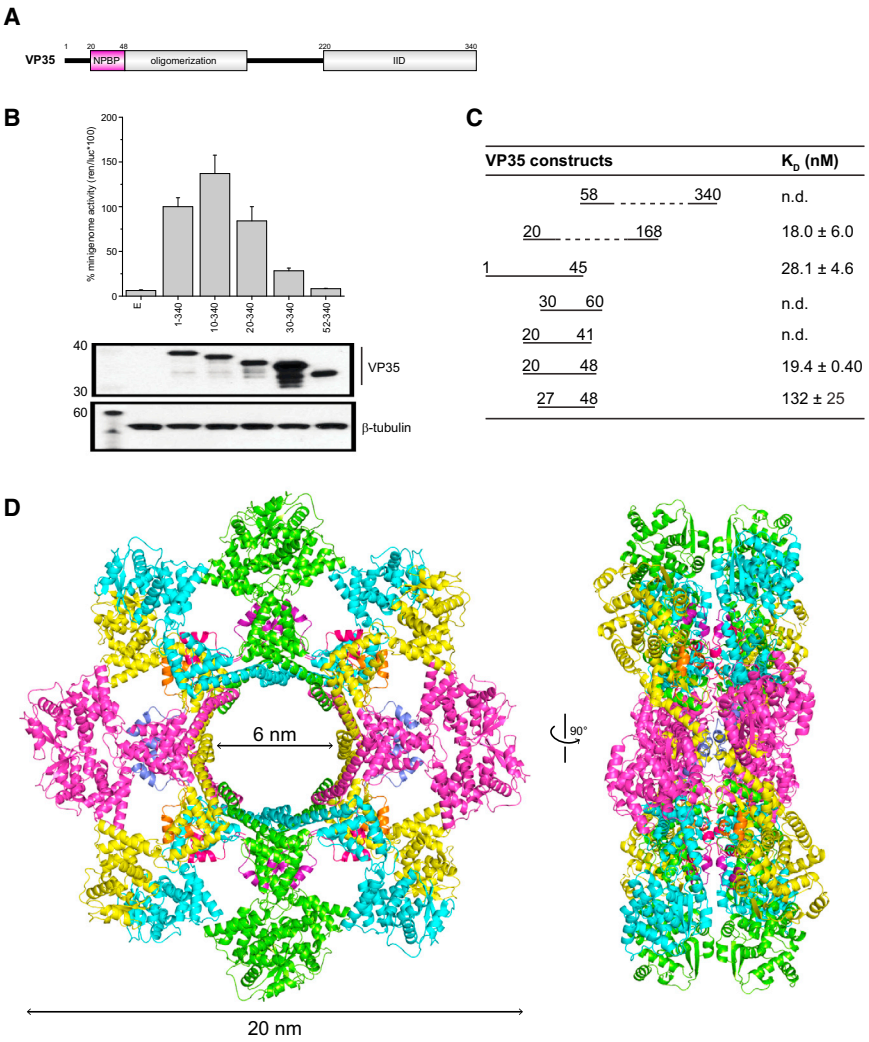

Figure 2. A Peptide Derived from EBOV Polymerase Co-factor VP35, Termed NPBP, Binds ΔNP_{NTD} with High Affinity and Specificity

(A) Domain organization of EBOV VP35, including an oligomerization and IID domains. There is a highly conserved region N-terminal to the oligomerization domain, residues 20–48, termed NPBP.

(B) Impact of the VP35 N terminus was evaluated by the Ebola minigenome assay. Ability of either WT or mutant VP35 proteins lacking various N-terminal sequences was tested and plotted as normalized minigenome activity, where WT VP35 activity was set to 100%. Below, representative western blots show similar levels of VP35 protein expression. β-tubulin was used as loading control. Error bars represent the SD from independent replicates.

(C) Summary of binding measurements by ITC between ΔNP_{NTD} and VP35 N-terminal truncation mutants reveal that residues 20–48 are necessary and sufficient for high-affinity binding. n.d., not determined.

(D) The structure of ΔNP_{NTD} in complex with VP35 NPBP peptide in a ribbon representation (left) and in a 90° rotated configuration (right). Each NPBP/ΔNP_{NTD} complex in the asymmetric unit is colored yellow/orange (mol A/mol E), magenta/blue (mol B/mol F), green/purple (mol C/mol G), and cyan/pink (mol D/mol H).

See also Figures S1D and S2–S4 and Table S1.

Peptides were subjected to quantitative analysis by isothermal titration calorimetry (ITC), and a summary of the results is shown in Figure 2C. These results revealed that VP35 residues 20–48 (i.e., NPBP) comprise the most critical region for high-affinity ΔNP_{NTD} binding (K_D = 18.0 ± 6.0 nM at 500 mM NaCl; Figures 2C and S2B; and K_D = 28.9 ± 6.4 nM at 150 mM NaCl; Figure S2C). VP35 peptides 1–45 and 27–48 resulted in 1.5- and 6.5-fold reduction in binding affinity relative to that of NPBP for ΔNP_{NTD} protein, which support the importance of the core NPBP peptide. In contrast to these observations, VP35 peptides 30–60 and 20–41 displayed significantly weaker binding to ΔNP_{NTD} (Figures 2C and S2C). Further analysis of the ITC data and MALS results indicates that NPBP binds to ΔNP_{NTD} with a 1:1 stoichiometry (Figure S2B) with a complex molecular weight corresponding to one molecule of ΔNP_{NTD} and one molecule of NPBP (Figure S2D). We also assessed the secondary structure of the NPBP peptide by circular dichroism (CD) spectroscopy, which revealed that NPBP and truncations of NPBP are intrinsically disordered in solution. However, the characteristic random coil sequence of NPBP can also form helical structure as the addition of trifluoroethanol (TFE) resulted in CD spectra with higher helical characteristics (Figure S2E). However, helical propensity alone is not sufficient to bind NP protein, as some peptides (for example, VP35 20–43) do not bind despite being helical in TFE-containing buffers (Figures S2C and S2E). Together, these results reveal that the residues encompassed by VP35 NPBP peptide are intrinsically disordered in solution but have a tendency to form helical structure, which may be critical for high-affinity binding to NP in the context of the full-length VP35 protein.

(D) Representative chromatograms for NP 20–550 WT (cyan) and Tyr21Ala/His22Ala double mutant (red). NP 25–550 (black) is shown as a comparison (500 mM NaCl). The arrow marks the void volume in (B)–(D).

(E and F) Minigenome activity assays using NP truncation and point mutations as indicated in the figure. (E) N-terminal residues, including Tyr21 and His22, are important for oligomerization, and mutation of these residues results in loss of MG activity. (F) Mutants lacking only the C terminus inhibit MG activity of full-length NP. Error bars represent the SD from independent replicates.

See also Figure S1.

Structure of the VP35 NPBP/ΔNP_{NTD} Complex

We solved the crystal structure of the VP35 NPBP/ΔNP_{NTD} complex to 3.7 Å resolution by selenomethionine single-wavelength anomalous dispersion (Se-SAD) and observed four NPBP/ΔNP_{NTD} heterodimers in the asymmetric unit (termed mol A, mol B, mol C, and mol D for ΔNP_{NTD} and mol E, mol F, mol G, and mol H for NPBP) (Figures 2D and S3A; Table S1). Analysis of crystal packing revealed that 16 copies of the NPBP/ΔNP_{NTD} complex form a back-to-back double ring with eight ΔNP_{NTD} molecules arranged in each ring and ~6-nm inner and 20-nm outer diameters (Figures 2D and S3B). The overall structure of ΔNP_{NTD} contains two identifiable lobes, a head lobe spanning NP residues 38 to 240 and a foot lobe from 244 to 383 that is connected together by a flexible hinge located within the head lobe (Figure S4). The head lobe contains 12 α helices, with two parallel β strands (β1 and β2), including the first β strand located at the beginning of the structured region of NP. The first 37 residues at the N terminus are unstructured. The foot lobe contains ten α helices with two short antiparallel β strands (β3 and β4). The last two helices (α21 and α22) of the foot lobe make structural contacts that are unique to EBOV NP (Figures S3B and S3C) when compared to other NNSV nucleoproteins (N). Specifically, these helices make extensive non-bonded contacts with helices α21 and α22 from n-1 and n+1 NP molecules, where n is one of the eight molecules that make up the ring (Figures S3B and S3C). The α21 and α22 α helices extend into the middle of the ring structure formed by symmetry related molecules. From the structure, the function of the ring configuration is unclear. However, previous data for other nucleoprotein molecules from NNSVs and previous electron microscopy studies of EBOV suggest that the ring configuration we observe here, where NP-NP interactions stabilize ring formation, may provide the intermolecular interactions to maintain NP-NP contacts in the Ebola virus nucleocapsid (Bharat et al., 2012).

NPBP Binds the Foot Lobe of ΔNP_{NTD}

All four ΔNP_{NTD} molecules are present in the structure. However, the head lobes of molecules B and D show a high degree of disorder with corresponding high average and individual B-factors (Table S1; Figure S3D). The B-factors indicate that the conformations of head lobes in symmetrically equivalent copies of these molecules across the crystal lattice differ in their orientation by 1–2 Å. In contrast, molecules A and C are well ordered (Figures 3A and S3D). Thus, in the analysis of intermolecular interactions between NPBP and ΔNP_{NTD}, we use the coordinates of mol G (NPBP) and mol C (ΔNP_{NTD}), respectively (Figure 3). In the structure of mol G/mol C, NPBP interacts exclusively with the foot lobe of ΔNP_{NTD}. NPBP forms two orthogonal helices (VP35 residues 26–36 form an α helix and residues 40–42 form a turn of a 3_{10} helix) and makes multiple hydrogen bonds and non-bonded contacts with NP (Figures 3B–3E). In an effort to validate the presence of NPBP peptide in our structure, we obtained additional NPBP/ΔNP_{NTD} complex crystals where the peptide was labeled at positions Met20 and Met34 with selenomethionine (SeMet) and the ΔNP_{NTD} was also SeMet labeled. Analysis of the diffraction data for one of these crystals revealed anomalous signal at the side chains of Met20 and Met34, which confirms that the peptide observed in the structure results from the VP35 NPBP (Figure 3C).

Next, we evaluated the interactions between NPBP and ΔNP_{NTD} at the molecular level by assessing surface electrostatics, hydrogen bonding, and non-bonded contacts. Evaluation of the NPBP and ΔNP_{NTD} in the complex suggest that there is limited charge complementarity (Figure 3D). Closer examination of the residue-specific binding interactions shows that nearly all the residues in the peptide (from residues 20 to 47) are within 4.5 Å of NP residues, which is consistent with the formation of a large binding interface with many important contacts that drive specificity and affinity (Figures 3E and 4A). The complementary binding interface from Ebola virus NP consists of helices α13, α14, and α15 and β3 and β4 strands, where NPBP wraps around the β3 and β4 beta strands (Figure 3E). All residues of NP that contribute to the binding interface are conserved across different Ebola viruses (Figure S1A). This interface contains ~2,600 $Å^2$ of shared buried surface area, of which ~1,200 $Å^2$ is contributed by NPBP. We also observe several important hydrogen bonds. For example NPBP residues Pro21, Gly22, Glu24, Ser26, Ser30, Glu31, and Phe44 are engaged in intermolecular H bonds with NP residues (Figure 4A). Interestingly, Arg37 from NPBP also makes an H bond with Glu292 from NP and the molecular interface formed by these bonds also further occlude the NPBP α helix from the solvent (Figure 4B). Collectively, these observations further support the specificity of the NPBP/NP interactions.

To further define the NPBP/ΔNP_{NTD} interface, NP residues were mutated to alanine and binding to VP35 NPBP in vitro and cell-based MG activity were assessed. Arg240 and Asp252, were important for VP35 NPBP interactions as the observed ITC-based binding affinities for the mutants are substantially lower than WT NP binding to NPBP (Figure 4C). Specific interactions between NPBP and NP also significantly depend on Lys248 as mutation of this residue to alanine results in near-complete loss of binding. We also tested the importance of these residues in the MG assay in order to confirm that Arg240, Lys248, and Asp252 are critical for viral RNA synthesis. Resulting data shown in Figure 4D reveals that mutations altering NPBP and NP binding impact Ebola virus RNA synthesis in the MG assay. Since these mutations are at the interface, a potential explanation is that these residues enhance the interaction between WT VP35 and NP.

ΔNP_{NTD} Binds ssRNA, and the ssRNA Binding Is Inhibited by NPBP

The ability of NP to bind RNA is well established (Bharat et al., 2012; Huang et al., 2002; Mühlberger et al., 1999; Noda et al., 2010, 2011; Watanabe et al., 2006). Therefore, we assessed if ΔNP_{NTD} can bind ssRNA and dsRNA. Using a dot blot assay, we find that NP selectively binds ssRNA (K_D = 620 ± 230 nM), whereas NP does not bind dsRNA (Figure 5A). Analysis of the NPBP/ΔNP_{NTD} structure identified several highly basic regions (Figure 3D). Using surface charge as a guide, we identified K160, K171, and K174 as potential ssRNA binding sites (Figure 5B). Mutation of these residues to alanine demonstrates their role in ssRNA binding (Figure 5C). In contrast, NP residues that are critical for NPBP binding and for EBOV

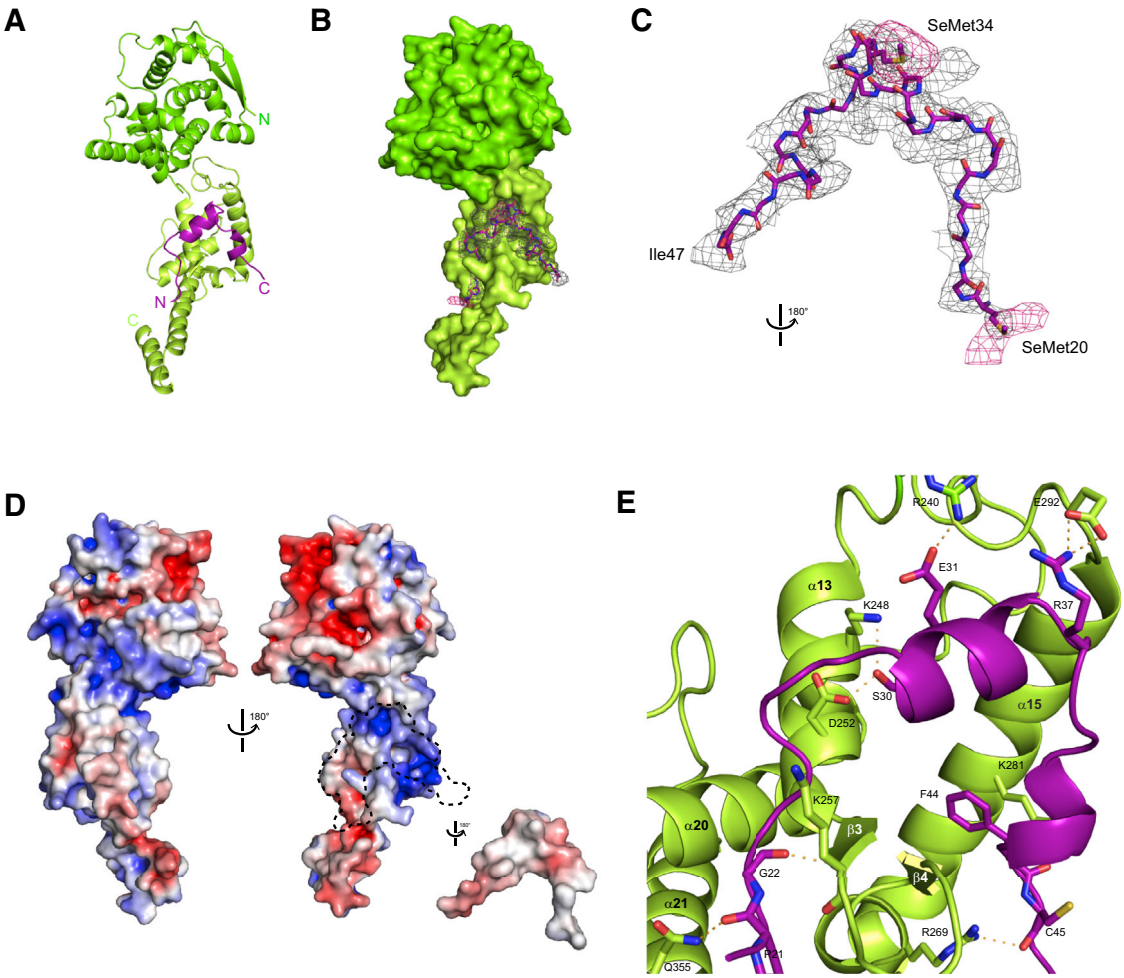

Figure 3. The Complex Structure of ΔNP_{NTD} and NPBP Reveals Extensive Intermolecular Interactions

(A) The 1:1 complex of NPBP/ΔNP_{NTD} (mol C/mol G). The ΔNP_{NTD} head lobe (residues 37–146, dark green) also contains a flexible hinge region (residues 147–239) that connects to the foot lobe (residues 240–285, light green). The VP35 NPBP interacts with the binding surface formed exclusively by the ΔNP_{NTD} foot lobe.

(B) Surface representation of ΔNP_{NTD} with a 1.0 sigma electron density (sigmaA weighted $2F_o$-F_c) mesh shown for NPBP.

(C) An anomalous difference map was calculated from data collected at the selenium edge on a crystal of SeMet derivatized ΔNP_{NTD} bound to NPBP synthesized with Se-Met instead of Met. Relative orientation of the figure as shown is 180° rotated from (B). The anomalous map (pink) is contoured at 3.0 sigma to show the position of selenium atoms in the methionine residues within the NPBP structure (Cα backbone shown in stick representation). Residues SeMet 20 and SeMet 34 are shown in stick representation.

(D) Analysis of the NPBP/ΔNP_{NTD} complex shows surface complementarity and extensive hydrophobic interactions among residues at the interface. Electrostatic surface representations of the NPBP/ΔNP_{NTD} complex with (left) and without NPBP (right). Red, white, and blue represent negative, neutral, and positive electrostatic potential, respectively (-10 to $+10$ k_BT e^{-1}). A dotted outline highlights the region where the VP35 NPBP binds to ΔNP_{NTD}.

(E) Residue-specific contacts between ΔNP_{NTD} and NPBP are highlighted by the amino acid side chains shown within 5 Å of NPBP.

See also Figures S2 and S4.

MG activity, such as R240, K248, and D252, are not important for ssRNA binding. Next we conducted competitive binding assays between ssRNA and NPBP, which revealed that VP35 NPBP and ssRNA can compete for binding to ΔNP_{NTD}. In these experiments, NPBP was titrated into the reaction while ssRNA and ΔNP_{NTD} concentrations were held constant. Increasing NPBP concentration resulted in a proportional loss of ssRNA from the ssRNA-NP complex (Figure 5D), yielding a half maximal inhibitory concentration (IC_{50}) of 4 μM. These results indicate that ssRNA and NPBP binding to NP are mutually exclusive.

EBOV NP alone forms oligomers and a putative function of VP35 is to maintain EBOV NP in an RNA-free non-oligomeric form. Initial cryo-electron microscopy (cryo-EM) studies revealed that NP_{NTD} (1–457) and WT NP (1–739) can form ring structures. Representative images for NP_{NTD} reveal that these protein oligomers can assemble into near-uniform rings, with an outer diameter of ~40 nm (Figure 6A). Individual images of different ring structures reveal the top and bottom conformation of these rings and provide side views. While the relevance of the double-ring conformation observed in the crystal structure is currently unclear (Figure 2D), our observation of double rings

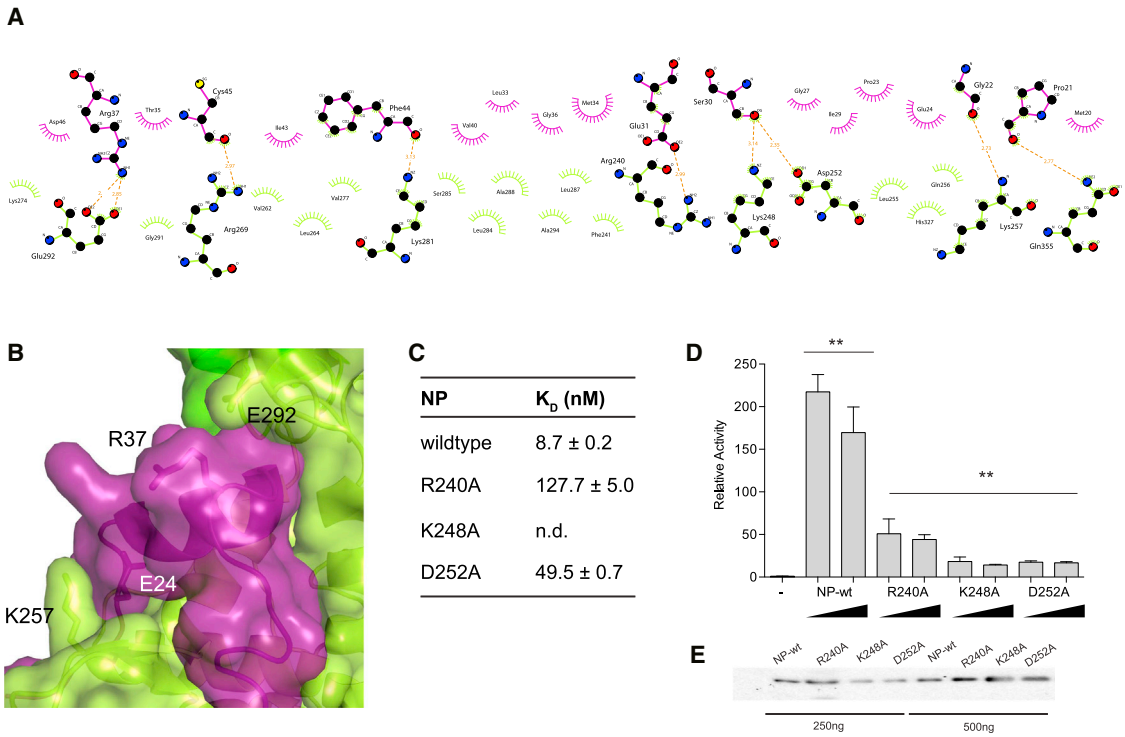

Figure 4. Mutational Analysis Validates the NPBP Binding Site on NP

(A) Non-bonded contacts drive NPBP/ΔNP_{NTD} binding. LigPlot^{+} diagram showing extensive hydrophobic and hydrogen bond interactions between ΔNP_{NTD} and NPBP. Protein side chains are shown as ball and sticks. Hydrogen bonds are shown as orange dotted lines. Non-bonded contacts are shown as spoked arcs.

(B) Surface and ribbon representation highlighting the interaction between NPBP (purple) and the foot lobe of ΔNP_{NTD} (light green). VP35 NPBP residues Glu24 and Arg37 and NP residues Lys257 and Glu292 are shown in stick representation.

(C) Summary of ITC binding measurements between MBP fusion ΔNP_{NTD} mutants and NPBP reveal that residues R240, K248, and D252 are involved in NPBP/ΔNP_{NTD} complex interactions. n.d., not determined.

(D) Impact of the NP mutants was evaluated by the MG assay. Ability of either WT or mutant NP proteins to promote MG activity were tested and plotted as MG activity relative to no NP control. The p values were determined by Student's t test. **$p < 0.001$. Representative western blots to show similar levels of NP protein expression. Error bars represent the SD from independent replicates.

(E) Representative western blots for NP proteins used in (D) at 250 and 500 ng plasmid transfections.

under distinct sample conditions by cryo-EM suggests that this conformation may be functionally important. However, in our crystal structure, crystal packing may impact the ring formation, since ΔNP_{NTD}/NPBP is a monomer in solution. Addition of NPBP to the cryo-EM sample results in loss of the ring conformation, presumably due to the formation of 1:1 heterodimers between NPBP and NP_{NTD} (Figure 6B). Taken together, our cryo-EM and X-ray results show that NPBP can cause morphological differences between the oligomeric ring structures formed by NP_{NTD} and NP_{NTD}/NPBP complexes. Next, we evaluated a variety of NP constructs, including ΔNP_{NTD} construct and NP_{NTD}, using size exclusion chromatography (SEC) as a measure of the hydrodynamic behavior of NP upon binding to NPBP under low- (150 mM) and high-NaCl (500 mM) buffer conditions. In contrast to previous results for the peptide-free NP proteins (Figures 1B and 1C), which eluted at the V_0, all NPBP-bound NP proteins eluted at a volume consistent with a well-behaved heterodimer (one molecule of NP and one NPBP molecule) (Figure 6C), indicating that NPBP interaction also prevents oligomerization.

VP35 NPBP Inhibits Ebola RNA Synthesis

In order to determine whether VP35 NPBP can function in *trans* to complement a VP35 protein lacking the NPBP region and support RNA synthesis, we tested various VP35 N-terminal truncation mutants together with plasmids expressing GFP-NPBP or using a cell-penetrating peptide fused to the NPBP sequence in the MG assay. Specifically, we fused the NPBP with an N-terminal TAT peptide (sequence YGRKKRRQRRR). In this assay, we used VP35 lacking the N-terminal 51 residues and assessed how addition of different regions of EBOV VP35 impact MG activity. Resulting data show that GFP-NPBP or other VP35 truncations (52–340) were nonfunctional in this assay, suggesting that the function of NPBP is required in *cis* with the rest of the VP35 polypeptide sequence (Figures 7A and S5A).

Given that NPBP occupies a functionally critical site on NP and is required for RNA synthesis, we next tested the ability of NPBP to inhibit Ebola virus RDRP activity. We used plasmid expressing GFP-NPBP and observed dose-dependent inhibition of MG activity by NPBP (GFP-NPBP) with an IC_{50} = 33 μM relative to a GFP peptide control (Figures 7B and S5B). We then tested

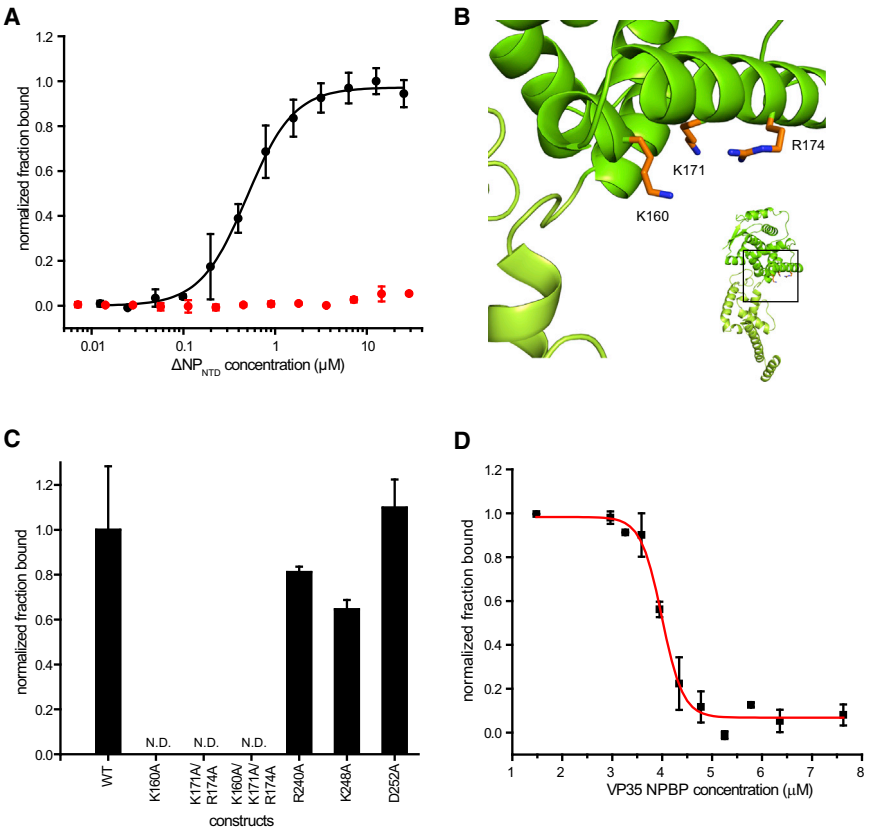

Figure 5. EBOV VP35 NPBP Binding Can Compete with NP-ssRNA Binding

(A) Measurement of the fraction of ^{32}P end-labeled ssRNA (20 base, black) and dsRNA (20 nucleotide base pair, red) bound to ΔNP_{NTD}. The ratio of ^{32}P captured on nitrocellulose (from protein bound RNA) or nylon membranes (free RNA) is shown normalized to the fraction bound. Error bars represent the SD from independent replicates.

(B) Ribbon representation of ΔNP_{NTD} from the ΔNP_{NTD}/NPBP complex structure (inset) highlighting several residues (stick representation) in one of the major basic patches that is important for ssRNA binding.

(C) Dot-blot binding results. Relative comparison of mutant NP proteins binding to 20 nt ssRNA compared to WT NP. Error bars represent the SD from independent replicates.

(D) ΔNP_{NTD} binding to 5 nM ssRNA as a function of VP35 NPBP concentration. Shown are representative data from at least three independent experiments. Error bars represent the SD from independent replicates.

how TAT-NPBP would function in a similar assay. These peptides were applied to cells prior to transfection with MG assay plasmids. Similar to the GFP-NPBP peptide, we observed dose-dependent inhibition of MG activity by Tat-NPBP, but not by the control peptide (Figures 7C and S5C).

To further test activity of NPBP in the context of EBOV infections, HeLa cells were pretransfected with the GFP-NPBP or GFP-control peptide constructs and then challenged with EBOV. Representative images of these infections show that GFP-NPBP, but not the GFP control plasmid, was able to inhibit EBOV replication (Figure 7D). Consistent with the immunofluorescence results and with the MG assays, qRT-PCR results show that the presence of GFP-VP35 NPBP, but not the GFP-control, results in lower levels of viral RNA in the cell supernatants (Figure 7E). Collectively, these results suggest that NPBP can interact with the NP in the viral RDRP complex and has the potential to inhibit viral RNA synthesis.

DISCUSSION

Here, we describe the identification and first characterization of the core regulatory elements from EBOV NP and VP35 proteins and their impact on viral RNA synthesis. NPBP, a peptide derived from EBOV VP35, is necessary and sufficient to maintain NP in a non-oligomeric and RNA-free state (NP^0), but NPBP cannot support viral RNA synthesis in *trans*. Our results support a model where Ebola VP35 NPBP binding to NP prevents NP from associating with noncognate RNA (i.e., cellular and non-genomic viral RNA). In addition, NPBP supports viral RNA synthesis in the context of full-length VP35, but in isolation, NPBP inhibits viral RNA synthesis.

In the structure of the ΔNP_{NTD}/NPBP complex, we observe several characteristics that are unique to the EBOV NP protein. First, the location of the VP35 peptide binding site is highly conserved in filoviruses. Second, upon binding, NP makes important contacts with NPBP, such as hydrogen bonds with Glu292, which induces the NPBP peptide forms an unusual kink facilitated by Thr35 and Gly36, which allows for a 3_{10} helical turn (Figure 3E). Third, the NP-NP association in the C-terminal lobe involves a helix-helix interaction that is not observed in any of the NNSV nucleoprotein structures to date (Figure S6). Finally, we do not observe electron density for ~75 residues at the C terminus of Ebola virus NP. We note that the sequence in this region (i.e., residues 380–450) has low sequence complexity and therefore may be in largely random coil conformation. This observation coupled with sequence alignments with other NNSVs suggest that the Ebola virus NP N-terminal domain may be smaller than previously recognized (Watanabe et al., 2006).

As Ebola virus NP protein is an integral part of the viral nucleocapsid and is intimately associated with the viral RNA template, its oligomeric state is of particular importance for maintaining template integrity and providing template access to the viral RDRP. Our data show that deletion of the N-terminal 24 residues or mutation of highly conserved Tyr21 and His22 to alanine in Ebola virus NP results in loss of oligomerization and corresponding loss of function in the MG assays. However, in addition to Tyr21 and His22, other residues within the first 40 amino acids of NP may be involved in facilitating NP-NP interactions.

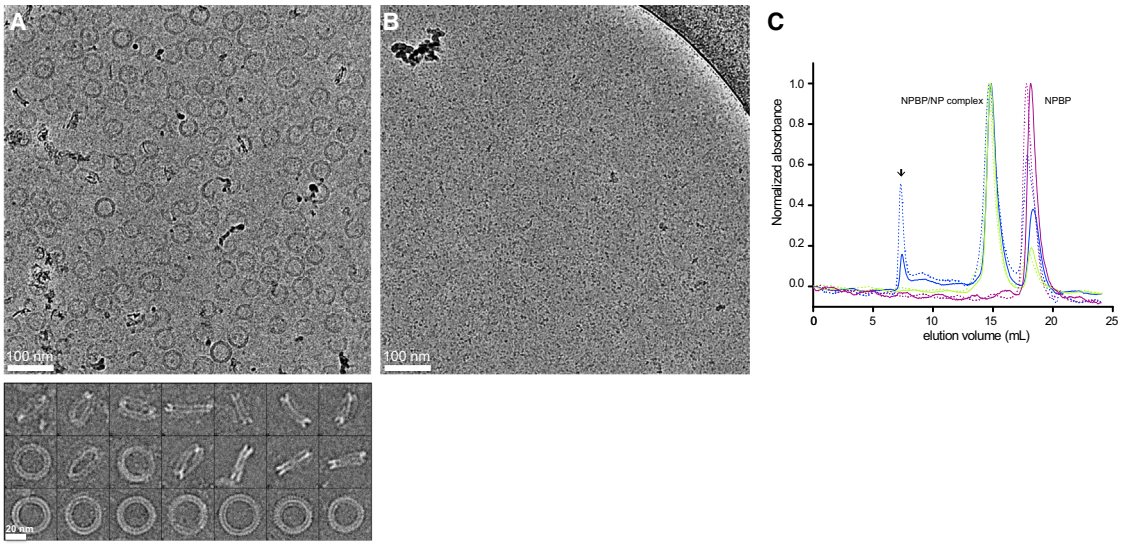

Figure 6. EBOV VP35 NPBP Binding Can Dismantle Oligomeric Ring Structures Formed by NP_{NTD}

(A) Representative cryo-EM images of NP_{NTD} forming double ring structures, observed from top and side views.

(B) Ring-like structures formed by NP_{NTD} disappear upon addition of NPBP peptide just prior to cryo-EM grid preparation.

(C) Representative chromatograms of NPBP complex of NP_{NTD} in 150 mM NaCl (blue dotted line) and 500 mM NaCl buffers (blue solid line), ΔNP_{NTD} in 150 mM NaCl (green dotted line), and 500 mM NaCl (green solid line) from size exclusion chromatography. NPBP peptide alone is shown in 150 mM NaCl (purple dotted line) and 500 mM NaCl (purple solid line) buffer conditions. Location of the void volume for the Superdex 200 column is indicated with an arrow.

The NP C terminus is dispensable for oligomerization, but not for viral RNA synthesis, as deletions C-terminal to residue 551 result in loss of Ebola RNA binding. Our observations are also consistent with previous studies, where a 150-residue deletion at the N terminus resulted in loss of NP-NP association (Watanabe et al., 2006). However, because such large deletions can result in the loss of structural integrity, it is difficult to attribute these results to a role for oligomerization. Our results also suggest that the NP-NP self-association is regulated by the region that binds NPBP (Figure 2A). Importantly, this binding and resulting change in the NP oligomeric state does not depend on the oligomeric state of VP35 (Möller et al., 2005; Reid et al., 2005) as we observe similar affinities between NP-VP35 and NP-NPBP (see Figures 2C and S2).

VP35 prevents high-affinity NP-RNA interactions until nascent NP reaches the site of viral RNA synthesis, where VP35 facilitates transfer of a monomeric and template-free NP (NP^0) to the viral template RNA, as our data show that VP35 NPBP binding releases RNA from NP. Upon binding to template RNA to form the NP-RNA complex, NP is released from interactions with VP35 NPBP through a yet-unknown mechanism. Release from NPBP and subsequent binding to viral RNA likely induces NP oligomerization, which can further stabilize the RNA-bound NP proteins. Our results, particularly data that show how NPBP can outcompete ssRNA binding, are consistent with a model where NPBP overrides NP-NP and NP-RNA interactions in order to maintain Ebola NP in the NP^0 state. Not surprisingly, deletion of the NPBP sequence from Ebola VP35 results in loss of viral RNA synthesis likely due to the lack of NP^0 to support viral RNA synthesis. However, when a truncated VP35 lacking NPBP (residues 52-340) was co-expressed with the VP35 NPBP peptide and other components in the MG assay, NPBP failed to support viral RNA synthesis in *trans*. In addition, proper viral RNA synthesis may require NPBP in the context of the full-length VP35 to bind NP to generate NP^0. Among the possible reasons for this outcome is a need for NPBP, which is located in the VP35 N terminus, to function together with VP35 C-terminal IID region. Our previous studies revealed that VP35 IID is also important for virus RNA synthesis. Specifically, we were able to show that conserved basic residues within the α-helical subdomain of VP35 IID were critical for VP35-NP interactions (Leung et al., 2009; Prins et al., 2010). Another possibility is that the NPBP binding to NP also provides a means to correctly localize the NP^0 proteins to the viral RDRP at a site near the viral nucleocapsid (NP-RNA). In such an arrangement, full-length VP35 can also provide template access to the polymerase L.

NNSV P and VP35 proteins are essential for viral RNA synthesis despite the lack of any sequence similarity among these proteins. The P protein, which is functionally equivalent to Ebola virus VP35, is thought to maintain newly synthesized nucleoprotein molecules in a non-oligomeric and RNA-free state (N^0). Studies on vesicular stomatitis virus (VSV) and Nipah virus (NiV) have shown that an N-terminal region of each respective P protein is sufficient to bind N^0. In addition, P peptide binding (N^0-P) presumably blocks RNA access to a groove formed between the N-terminal and C-terminal lobes of nucleoprotein based upon structural alignments of the N^0-P and N-RNA complex structures. Comparison of the NP structure from our Ebola virus ΔNP_{NTD}/NPBP complex with corresponding structures of VSV (Leyrat et al., 2011a, 2011b) and NiV N (Yabukarski et al., 2014) in complex with the P-derived peptide (N^0-P), analogous to the Ebola VP35 NPBP, reveals several differences. The P peptide binding site and the secondary structure of the P peptide are different from Ebola virus VP35 NPBP bound to NP (Figure S6). In

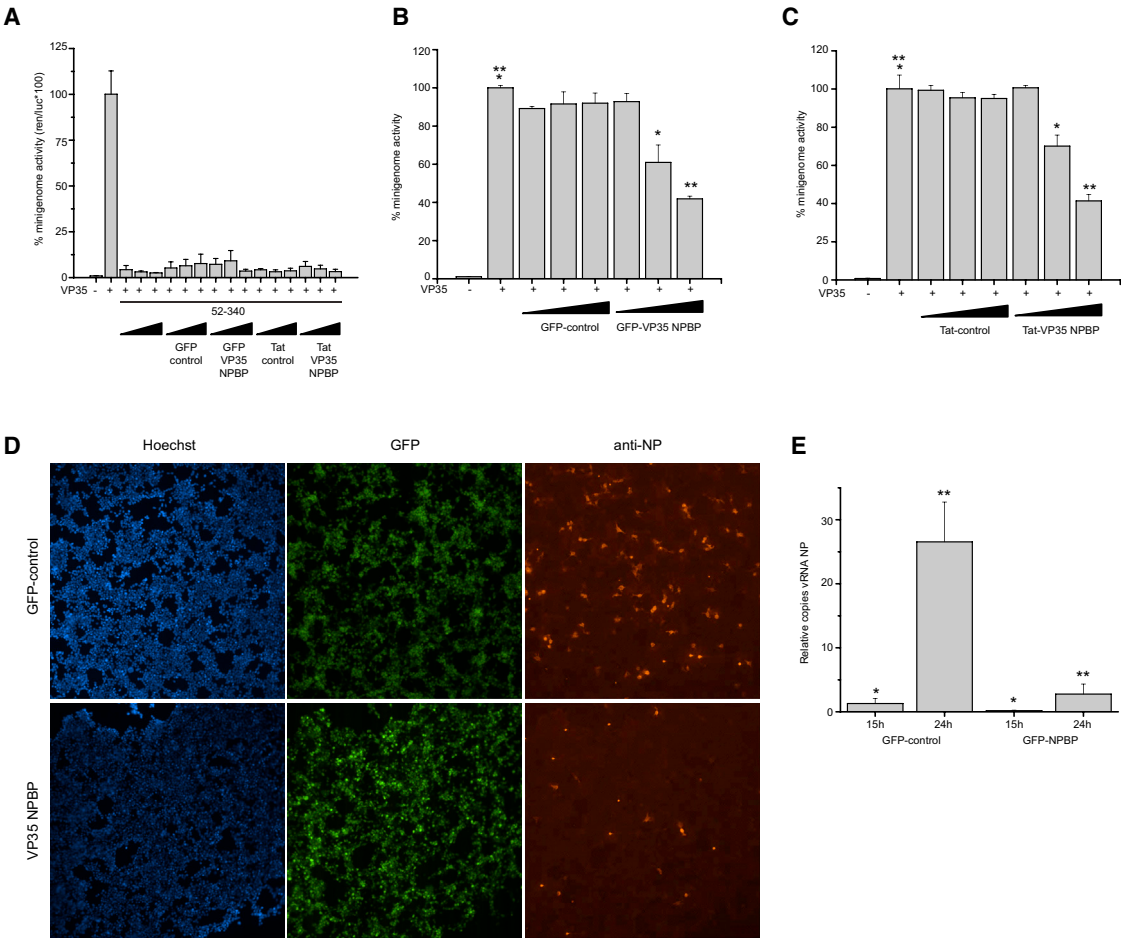

Figure 7. VP35 NPBP Inhibits EBOV Replication

(A) NPBP in the context of VP35, but not as an isolated peptide, can support RNA synthesis. MG assay performed with VP35 52–340 with additional VP35 truncations, as indicated in the figure, failed to support RNA synthesis. 500 ng of GFP-NPBP and 100 μM of TAT-NPBP were used. Error bars represent the SD from independent replicates.

(B and C) Representative results from MG assay with either (B) GFP control plasmid or GFP-NPBP peptide expressing plasmid with three different doses (125, 250, and 500 ng; *p = 0.04, **p = 0.001). (C) Control TAT-peptide or TAT-NPBP (1, 10, and 100 μM). Activity in (A)–(C) is reported as a percent of the average activity recorded for WT VP35 (*p = 0.01, *p = 0.002). The p values were determined by Student's t test. Error bars represent the SD from independent replicates.

(D) VP35 NPBP inhibits EBOV infection in HeLa cells. Cells were transfected with either plasmid encoding GFP-NPBP peptide fusion (top) or GFP expressing plasmid (bottom) and then challenged with Zaire Ebola virus at an MOI of 0.05 48 hr after plasmid transfection. Representative images show cell nuclei stained with Hoechst 33342 dye (blue), plasmid expression (green), and virus replication (red, stained with anti-Ebola NP mAb).

(E) qRT-PCR analysis for GFP or GFP-NPBP (VP35 residues 20–48) expressing cells that were infected with Ebola virus. At 15 hr and 24 hr post-infection, supernatant was collected, TRIzol treated, and subjected to reverse transcription using a primer a complementary to the negative-sense viral RNA (vRNA) followed by qRT-PCR using primers directed to EBOV NP (*p = 0.06, **p = 0.006). The p values were determined by Student's t test. Error bars represent the SD from independent replicates.

See also Figures S5 and S6.

addition, there are intra-peptide interactions that stabilize the NPBP-bound conformation and are absent in the corresponding VSV- and NiV N-bound peptides. Moreover, in VSV and NiV, the N-N contacts are different from those observed for Ebola virus NP-NP. Specifically, we observe inter-NP interactions (see Figures S3B and S3C) that occur via helices in the foot lobe whereas the inter-N interactions in the VSV and NiV occur mainly via loop-loop interactions. Despite these structural differences, we observe several similarities. VSV and NiV N proteins and Ebola virus NP have similar folds and display similar domain arrangements in the first ~350–400 residues of each protein. In addition, our ΔNP_{NTD}/NPBP structure along with ssRNA binding studies show that NPBP binding is incompatible with RNA binding. Comparison of the ΔNP_{NTD}/NPBP structure from the current study with ssRNA-bound structures of VSV and RSV nucleoproteins suggest that the highly basic region highlighted in Figure 3D (left) may recognize and bind ssRNA in Ebola NP. Our results also show that the VP35 NPBP binding relieves NP oligomerization and NP-RNA binding by interacting with two distinct regions within NP that are important for viral RNA synthesis. These sites

on EBOV NP do not appear to overlap, since mutations of individual residues important for ssRNA binding and for NPBP binding appear to function independently. In contrast, structural alignments of the N^0-P and N-RNA structures suggest that P peptide binding to N protein in VSV and NiV may also limit N-RNA interactions by steric hindrance (Leyrat et al., 2011a; Yabukarski et al., 2014). Collectively, these results suggest that NNSVs may use variations of a common mechanism to control viral RNA synthesis.

Our results here show for the first time how EBOV VP35 uses the NPBP region to control viral RNA synthesis and highlight NNSV-common and filoviral-specific mechanisms by which EBOV VP35 regulates NP-NP and NP-RNA template interactions. These results also provide the framework to develop anti-viral therapeutics that target filoviruses.

EXPERIMENTAL PROCEDURES

Cloning and Purification

Ebola virus NP and VP35 constructs were subcloned into a modified pET15b (Novagen) vector containing a maltose binding protein fusion tag and TEV protease site and expressed in BL21(DE3) *Escherichia coli* cells grown at 37°C. Cells were induced for 12–14 hr at 18°C with 0.5 mM isopropyl β-D-1-thiogalactopyranoside and harvested at 8,000 × *g* for 10 min, resuspended in buffer A (20 mM Tris [pH 7.5], 1 M or 150 mM NaCl for NP and VP35, respectively), 20 mM imidazole (pH 7), 5 mM β-mercaptoethanol, and a protease inhibitor. Cells were lysed using an Avestin C3 homogenizer, clarified by centrifugation at 47,000 × g for 30 min, and supernatant was purified by affinity and ion-exchange chromatography. Fusion tags were removed by TEV protease cleavage and purified by ion exchange columns prior to final size-exclusion column. VP35 peptides were purchased from GenScript.

Selenomethionine-Labeled Protein

Proteins were expressed in M9-minimal media, supplemented with appropriately labeled metabolites, and purified in a manner similar to native protein described above.

Isothermal Titration Calorimetry

NP and VP35 binding was measured by VP-ITC microcalorimeter (MicroCal/GE Healthcare). Samples were dialyzed overnight at 25°C against 1 l of buffer B (20 mM Tris [pH 7.5], 500 mM NaCl, and 2 mM tris(2-carboxyethyl)phosphine [TCEP]). Raw ITC data were processed using Origin software and data fit by non-linear least-squares analysis to yield K_D (equilibrium binding constant) and *n* (number of binding sites). A representative of two to four independent experiments is shown.

SEC-MALS

SEC-MALS experiments were performed using a DAWN-HELEOS II detector (Wyatt Technologies) coupled to a Superdex SD200 column (GE Healthcare) in buffer C (20 mM Tris [pH 7.5], 250 mM NaCl, and 2 mM TCEP). 2 mg/ml sample was injected and raw data were analyzed using ASTRA 6 software (Wyatt Technologies) to determine the weight averaged molecular mass (M_W). Protein concentrations were determined using the refractive index measured by an Optilab T-rEX (Wyatt Technologies) and a dn/dc = 0.185 ml × g^{-1}.

Minigenome Assays

BSRT7 cells were co-transfected by using Lipofectamine 2000 (Invitrogen) with T7-driven expression plasmids encoding the EBOV NP, L, VP30, and VP35 proteins along with plasmid expressing a T7 promoter-driven EBOV minigenome RNA, which encodes a *Renilla* luciferase reporter gene and constitutively expressing firefly luciferase expression plasmid that served as a transfection control. At 24 hr posttransfection, cells were lysed with passive lysis buffer (Promega) and reporter activities were determined using the Dual Luciferase assay kit (Promega). *Renilla* luciferase activity was normalized to firefly luciferase activity. Minigenome reporter activation was expressed as percent minigenome activity setting activity of WT VP35 as 100%. Error bars represent the SD from three independent replicates.

Crystallization, Data Collection, and Structure Solution

ΔNP_{NTD} and VP35 NPBP were incubated together in 1:1 molar ratio prior to loading onto a Superdex SD200 column (GE Healthcare) with buffer containing 20 mM Tris (pH 7), 250 mM NaCl, and 2 mM TCEP. NPBP/ΔNP_{NTD} complex crystals were generated using the hanging-drop vapor diffusion method and streak seeding in well solution containing 100 mM Tris (pH 7.2), 50 mM HEPES (pH 7), and 23% PEG400. Crystals were cryoprotected in stabilization solution containing 100 mM Tris (pH 7.2), 50 mM HEPES (pH 7), 50 mM NaCl, 2 mM TCEP, 15% PEG400, and 15% PEG3350 followed by vitrification in liquid nitrogen.

X-ray data were collected at the Structural Biology Center 19ID at the Advanced Photon Source (Argonne, IL), Datasets from two crystals of SeMet derivatized NP protein bound to native VP35 NPBP were collected at low remote energy to minimize radiation damage with an oscillation angle of 0.8 and a crystal-to-detector distance of 500 mm. Dataset from one crystal of SeMet derivatized NP bound to SeMet derivatized VP35 NPBP was collected at the Se absorption peak to maximize the anomalous signal with an oscillation angle of 0.8 and a crystal-to-detector distance of 450 mm.

The structure of Ebola virus VP35 NPBP/ΔNP_{NTD} complex was solved using the diffraction data obtained from three crystals. The partial model was built using phases obtained from the averaging datasets of these crystals. The data averaging took the differences in the levels of anomalous signal into account. HKL3000 was used to process diffraction data sets for all crystals (Minor et al., 2006; Otwinowski and Minor, 1997). Computational corrections for absorption in a crystal and imprecise calculations of the Lorentz factor resulting from a minor misalignment of the goniostat were applied (Borek et al., 2003; Otwinowski et al., 2003). Anisotropic diffraction was corrected to adjust the error model and to compensate for the phasing signal for radiation-induced increase of non-isomorphism within the crystal (Borek et al., 2007, 2010, 2013). The data statistics are presented in Table S1. The crystals diffracted anisotropically to a resolution of 3.7 Å in the best direction and 4.0 and 4.2 Å in the other two directions. The estimated level of anomalous signal was 3.6% of the native intensity. We performed a search for heavy atom positions to a resolution of 7.0 Å with ShelxD (Sheldrick, 2008), which identified 28 Se positions with correlation coefficients: CCAll = 54.79% and CCWeak = 28.18%. The handedness of the solution was determined with ShelxE by analyzing the connectivity and contrast of the electron density maps. 26 Se positions were refined anisotropically to 4.4 Å with MLPHARE (Otwinowski, 1991), with the final FOM reaching 0.205. 4-fold NCS was identified by Resolve (Terwilliger, 2003, 2004). NCS averaging and solvent flattening was performed by DM (Cowtan and Main, 1998). The resulting electron density map was used for model building, which consisted of several cycles of BUCCANEER (Cowtan, 2006). Intermediate models from different cycles of BUCCANEER were combined manually into a more complete model for one of the four chains, which had the lowest thermal motions. This model was subsequently propagated by applying the NCS operators, and then iterative model building was repeated. The resulting oligomer was then manually rebuilt and corrected by iterative application of Coot, Refmac (Emsley and Cowtan, 2004; Murshudov et al., 1997, 1999) along with the local NCS restraints, jelly body refinement, and in the later cycles with TLS refinement (Winn et al., 2003).

The ΔNP_{NTD} chains in the asymmetric unit have different levels of order, with average B-factors for chains A, B, C, and D of 123, 190, 90, and 234 $Å^2$, respectively. Although the N-terminal domains for chains B and D could not be accurately modeled, the order of chains A and C was sufficient to build the entire peptide chain that consists of N-terminal head lobe and C-terminal foot lobe. SeMet positions for the ΔNP_{NTD} protein together with the SeMet-derivatized NPBP dataset analyzed separately provided unambiguous tracing for the ΔNP_{NTD} chains and NPBP chains. This model was propagated through an NCS symmetry operator and provides a credible indication as to where the N-terminal domains of chains B and D are located. However, due to their large thermal motions (equivalent to 1–2 Å shift of subdomains), the validation

statistics, which analyze how this region fits to the electron density, are not meaningful. The model was refined with these domains, because the electron density and packing interactions indicate where the domains are located, albeit the individual secondary structure elements can barely be fitted. All atomic interactions are analyzed based on the chains C and G.

Cryo-EM Specimen Preparation and Data Acquisition

The 400-mesh R1.2/1.3 holey carbon Quantifoil grid (Quantifoil Micro Tools GmbH) was cleaned with acetone (Sigma-Aldrich) for 12 hr and glow discharged before use. A 3.0-μl aliquot of purified Ebola NP oligomer at ~2 mg/ml in the presence or absence of 0.5 μl disruption peptide was applied to the grid, blotted for 8 s, and immediately frozen in liquid ethane using a Leica EM GP (Leica Microsystems) with temperature held constantly at 10°C and 99% humidity during the process. The grid was stored in liquid nitrogen until imaging. All grids were examined on a JEM 2100 (LaB_6 gun) cryo-electron microscope (JEOL) operated at 200 kV, spot size of 2, condenser aperture of 70 μm, and objective aperture of 60 μm. Images were recorded under low-dose condition on a Gatan 4k × 4k CCD camera (Gatan) at ×50,000 microscope magnification (corresponding to a calibrated sampling of 2.16 Å/pixel) and a dose of 50–60 electrons/$Å^2$ with defocus ranging from 3 to 5 μm. Particle images were manually boxed and extracted using EMAN2 (Tang et al., 2007) program with a box size of 288 × 288 pixels.

Structural Figure Generation and Analysis

Surface area and surface complementarity were calculated using AREAIMOL and *Sc*, respectively, as implemented in CCP4 program suite (CCP4, 1994). Structure figures were prepared using PyMOL (DeLano, 2002). Protein-protein interactions were analyzed using LigPlot$^+$ (Laskowski and Swindells, 2011). Topology diagrams were generated by PDBSum (Laskowski, 2007) and TopDraw (Bond, 2003). Sequence alignment was performed using ClustalW (Thompson et al., 2002) and prepared using ESPript 3.0 (Gouet et al., 2003).

RNA Binding and Competition Assays

20-nt ssRNA was labeled at the RNA 5′ using ^{32}P-γ-ATP. 25 μM of ΔNP_{NTD} was serially diluted and incubated with ^{32}P-20 nt ssRNA at 5 nM for 15 min prior to loading onto a dot blot apparatus (Bio-Rad). For peptide-competition experiments, 20 μM of VP35 NPBP was serially diluted and incubated with ΔNP_{NTD} at 4 μM for 30 min prior to the addition of ^{32}P-20 nt ssRNA (at 5 nM). The protein-RNA complex was then passed through nitrocellulose (NC) and nylon (NY) membranes. The membranes were scanned using a Typhoon 9410 Variable Model Imager, and the amount of ^{32}P-20 nt ssRNA bound to NC and NY membranes was quantified from the radioactivity detected. Data analyzed by Origin and the fraction ssRNA bound to ΔNP_{NTD} proteins were calculated using the equation shown below:

$$\text{fraction bound} = \frac{\text{RNA bound to NC}}{\text{RNA bound to NC} + \text{RNA bound to NY}}.$$

Virus Infection

HeLa cells were transfected with either a plasmid encoding GFP-NPBP peptide fusion or a GFP control expressing plasmid. 24 hr after plasmid transfection, cells were transferred to the BSL-4 laboratory and challenged with Zaire EBOV at an MOI of 0.05 and were fixed by immersing in neutral buffered formalin overnight. Fixed cells were washed three times with PBS and then stained with anti-Ebola-GP antibody followed by an anti-mouse-546 (Alexa) secondary antibody, nuclei were stained with Hoechst-33342 (Life-Technologies; 1:50,000 dilution). Cells were imaged on a Nikon Ti Eclipse microscope. Total cells (blue), transfected cells (green; GFP), and Ebola-infected cells (red; GP-specific mAb) were counted using CellProfiler software (Broad Institute) using customized pipelines, which are available from R.A.D. upon request.

qRT-PCR

293T cells were transfected with GFP or VP35 NPBP and infected with Zaire EBOV. At 15 and 24 hr postinfection, supernatant and cells were collected for RNA isolation using TRIZOL. For reverse transcription, either an oligo(dT) primer (for detection of mRNA) or a primer complementary to the negative-sense viral RNA (vRNA) was used, followed by quantitative real-time PCR using primers directed against NP. In parallel, qRT-PCR directed against β-actin mRNA was performed, to control for differences in the amount of total input RNA. The relative copy number of target RNA was calculated from the change in threshold cycle (CT) value between β-actin mRNA and target RNA. mRNA was reverse transcribed using a vRNA specific primer (NP), followed by quantitative real-time PCR using NP-specific primers. Shown are the means and SE from two independent experiments.

ACCESSION NUMBERS

Coordinates and structure factors have been deposited in to the PDB and are available under accession number 4YPI.

SUPPLEMENTAL INFORMATION

Supplemental Information includes Supplemental Experimental Procedures, six figures, and one table and can be found with this article online at http://dx.doi.org/10.1016/j.celrep.2015.03.034.

AUTHOR CONTRIBUTIONS

D.W.L., C.F.B., and G.K.A. conceived and designed the overall study. D.W.L. defined VP35 NPBP. D.W.L., J.M.B., and G.K.A. developed NP purification methods. J.P. purified proteins for crystallization. D.W.L. identified and optimized crystallization conditions and acquired crystallographic data, which was used by D.B. and Z.O. to solve the structure and build and refined the model. D.W.L., D.B., Z.O., C.F.B., and G.K.A. conducted analysis of the structure and designed validation assays. D.W.L., G.L., and G.K.A. designed and conducted RNA binding studies. I.H. conducted peptide analysis. P.L., R.S.S., and C.F.B. designed functional validation assays. P.L. and A.E.-F. conducted cell-based studies and analyzed results. Z.S. and W.C. conducted cryo-EM studies. M.A. and R.A.D. designed and executed BSL4 studies. D.W.L., D.B., C.F.B., and G.K.A. wrote the manuscript with input from all co-authors. All authors analyzed results and approved the submission.

ACKNOWLEDGMENTS

We thank Drs. T. Ellenberger, D. Fremont, T. Brett, N. Tolia, W. Li, and J. Payton for discussions; members of the G.K.A./G.L. W.C., C.F.B., and R.A.D. laboratories for experimental support; and Drs. S. Ginell, N. Duke, and J. Lazarz at Advanced Photon Source (APS) Sector 19 for beamline access and assistance during data collection. Use of Structural Biology Center beamlines at the APS is supported by the US DOE under contract DE-AC02-06CH11357. Use of the National Magnetic Resonance Facility at Madison is supported by NIH grant P41GM103399. This work was supported in part by a contract to the Center for Structural Genomics of Infectious Diseases (CSGID) from the NIAID/NIH/DHS (contract number HHSN272201200026C, Anderson-PI) to Z.O., by DOD grants DTRA 1-21-1-0002 to R.A.D., DTRA-HDTRA1-12-1-0051 and DTRA HDTRA1-14-1-0013 to C.F.B. and G.K.A., and by NIH grants (R01AI107056 to D.W.L.; R01GM053163 to Z.O.; R01AI077519 to R.A.D.; R01AI059536 to C.F.B.; U19AI109945 [Basler-PI] to C.F.B., D.W.L., and G.K.A.; and U19AI109664 [Basler-PI] to D.W.L., D.B., C.F.B. and G.K.A.; U19 AI070489 [Holtzman-PI], P41GM103832, and P50 GM1003297 to W.C.; and R01AI081914 to G.K.A.).

Received: December 8, 2014
Revised: February 18, 2015
Accepted: March 12, 2015
Published: April 9, 2015

REFERENCES

Basler, C.F., Mikulasova, A., Martinez-Sobrido, L., Paragas, J., Mühlberger, E., Bray, M., Klenk, H.D., Palese, P., and García-Sastre, A. (2003). The Ebola virus

VP35 protein inhibits activation of interferon regulatory factor 3. J. Virol. *77*, 7945–7956.

Bharat, T.A., Noda, T., Riches, J.D., Kraehling, V., Kolesnikova, L., Becker, S., Kawaoka, Y., and Briggs, J.A. (2012). Structural dissection of Ebola virus and its assembly determinants using cryo-electron tomography. Proc. Natl. Acad. Sci. USA *109*, 4275–4280.

Bond, C.S. (2003). TopDraw: a sketchpad for protein structure topology cartoons. Bioinformatics *19*, 311–312.

Borek, D., Minor, W., and Otwinowski, Z. (2003). Measurement errors and their consequences in protein crystallography. Acta Crystallogr. D Biol. Crystallogr. *59*, 2031–2038.

Borek, D., Ginell, S.L., Cymborowski, M., Minor, W., and Otwinowski, Z. (2007). The many faces of radiation-induced changes. J. Synchrotron Radiat. *14*, 24–33.

Borek, D., Cymborowski, M., Machius, M., Minor, W., and Otwinowski, Z. (2010). Diffraction data analysis in the presence of radiation damage. Acta Crystallogr. D Biol. Crystallogr. *66*, 426–436.

Borek, D., Dauter, Z., and Otwinowski, Z. (2013). Identification of patterns in diffraction intensities affected by radiation exposure. J. Synchrotron Radiat. *20*, 37–48.

Collaborative Computational Project, Number 4 (1994). The CCP4 suite: programs for protein crystallography. Acta Crystallogr. D Biol. Crystallogr. *50*, 760–763.

Cowtan, K. (2006). The Buccaneer software for automated model building. 1. Tracing protein chains. Acta Crystallogr. D Biol. Crystallogr. *62*, 1002–1011.

Cowtan, K., and Main, P. (1998). Miscellaneous algorithms for density modification. Acta Crystallogr. D Biol. Crystallogr. *54*, 487–493.

DeLano, W.L. (2002). The PyMOL Molecular Graphics System (DeLano Scientific).

Dziubańska, P.J., Derewenda, U., Ellena, J.F., Engel, D.A., and Derewenda, Z.S. (2014). The structure of the C-terminal domain of the Zaire ebolavirus nucleoprotein. Acta Crystallogr. D Biol. Crystallogr. *70*, 2420–2429.

Elliott, L.H., Sanchez, A., Holloway, B.P., Kiley, M.P., and McCormick, J.B. (1993). Ebola protein analyses for the determination of genetic organization. Arch. Virol. *133*, 423–436.

Emsley, P., and Cowtan, K. (2004). Coot: model-building tools for molecular graphics. Acta Crystallogr. D Biol. Crystallogr. *60*, 2126–2132.

Feng, Z., Cerveny, M., Yan, Z., and He, B. (2007). The VP35 protein of Ebola virus inhibits the antiviral effect mediated by double-stranded RNA-dependent protein kinase PKR. J. Virol. *81*, 182–192.

Gouet, P., Robert, X., and Courcelle, E. (2003). ESPript/ENDscript: Extracting and rendering sequence and 3D information from atomic structures of proteins. Nucleic Acids Res. *31*, 3320–3323.

Hartman, A.L., Towner, J.S., and Nichol, S.T. (2004). A C-terminal basic amino acid motif of Zaire ebolavirus VP35 is essential for type I interferon antagonism and displays high identity with the RNA-binding domain of another interferon antagonist, the NS1 protein of influenza A virus. Virology *328*, 177–184.

Huang, Y., Xu, L., Sun, Y., and Nabel, G.J. (2002). The assembly of Ebola virus nucleocapsid requires virion-associated proteins 35 and 24 and posttranslational modification of nucleoprotein. Mol. Cell *10*, 307–316.

Laskowski, R.A. (2007). Enhancing the functional annotation of PDB structures in PDBsum using key figures extracted from the literature. Bioinformatics *23*, 1824–1827.

Laskowski, R.A., and Swindells, M.B. (2011). LigPlot+: multiple ligand-protein interaction diagrams for drug discovery. J. Chem. Inf. Model. *51*, 2778–2786.

Leung, D.W., Ginder, N.D., Fulton, D.B., Nix, J., Basler, C.F., Honzatko, R.B., and Amarasinghe, G.K. (2009). Structure of the Ebola VP35 interferon inhibitory domain. Proc. Natl. Acad. Sci. USA *106*, 411–416.

Leung, D.W., Prins, K.C., Basler, C.F., and Amarasinghe, G.K. (2010a). Ebolavirus VP35 is a multifunctional virulence factor. Virulence *1*, 526–531.

Leung, D.W., Prins, K.C., Borek, D.M., Farahbakhsh, M., Tufariello, J.M., Ramanan, P., Nix, J.C., Helgeson, L.A., Otwinowski, Z., Honzatko, R.B., et al. (2010b). Structural basis for dsRNA recognition and interferon antagonism by Ebola VP35. Nat. Struct. Mol. Biol. *17*, 165–172.

Leyrat, C., Jensen, M.R., Ribeiro, E.A., Jr., Gérard, F.C., Ruigrok, R.W., Blackledge, M., and Jamin, M. (2011a). The N(0)-binding region of the vesicular stomatitis virus phosphoprotein is globally disordered but contains transient α-helices. Protein Sci. *20*, 542–556.

Leyrat, C., Yabukarski, F., Tarbouriech, N., Ribeiro, E.A., Jr., Jensen, M.R., Blackledge, M., Ruigrok, R.W., and Jamin, M. (2011b). Structure of the vesicular stomatitis virus N^0-P complex. PLoS Pathog. *7*, e1002248.

Luthra, P., Ramanan, P., Mire, C.E., Weisend, C., Tsuda, Y., Yen, B., Liu, G., Leung, D.W., Geisbert, T.W., Ebihara, H., et al. (2013). Mutual antagonism between the Ebola virus VP35 protein and the RIG-I activator PACT determines infection outcome. Cell Host Microbe *14*, 74–84.

Masters, P.S., and Banerjee, A.K. (1988). Complex formation with vesicular stomatitis virus phosphoprotein NS prevents binding of nucleocapsid protein N to nonspecific RNA. J. Virol. *62*, 2658–2664.

Minor, W., Cymborowski, M., Otwinowski, Z., and Chruszcz, M. (2006). HKL-3000: the integration of data reduction and structure solution—from diffraction images to an initial model in minutes. Acta Crystallogr. D Biol. Crystallogr. *62*, 859–866.

Möller, P., Pariente, N., Klenk, H.D., and Becker, S. (2005). Homo-oligomerization of Marburgvirus VP35 is essential for its function in replication and transcription. J. Virol. *79*, 14876–14886.

Mühlberger, E. (2007). Filovirus replication and transcription. Future Virol *2*, 205–215.

Mühlberger, E., Weik, M., Volchkov, V.E., Klenk, H.D., and Becker, S. (1999). Comparison of the transcription and replication strategies of marburg virus and Ebola virus by using artificial replication systems. J. Virol. *73*, 2333–2342.

Murshudov, G.N., Vagin, A.A., and Dodson, E.J. (1997). Refinement of macromolecular structures by the maximum-likelihood method. Acta Crystallogr. D Biol. Crystallogr. *53*, 240–255.

Murshudov, G.N., Vagin, A.A., Lebedev, A., Wilson, K.S., and Dodson, E.J. (1999). Efficient anisotropic refinement of macromolecular structures using FFT. Acta Crystallogr. D Biol. Crystallogr. *55*, 247–255.

Noda, T., Halfmann, P., Sagara, H., and Kawaoka, Y. (2007). Regions in Ebola virus VP24 that are important for nucleocapsid formation. J. Infect. Dis. *196* (*2*), S247–S250.

Noda, T., Hagiwara, K., Sagara, H., and Kawaoka, Y. (2010). Characterization of the Ebola virus nucleoprotein-RNA complex. J. Gen. Virol. *91*, 1478–1483.

Noda, T., Kolesnikova, L., Becker, S., and Kawaoka, Y. (2011). The importance of the NP: VP35 ratio in Ebola virus nucleocapsid formation. J. Infect. Dis. *204* (*3*), S878–S883.

Otwinowski, Z. (1991). Maximum likelihood refinement of heavy atom parameters. In: Isomorphous Replacement and Anomalous Scattering. Proceedings of the CCP4 Study Weekend, 25–26 January 1991, W. Wolf, P.R. Evans, and A.G.W. Leslie, eds. (Science and Engineering Research Council), pp. 80–85.

Otwinowski, Z., and Minor, W. (1997). Processing of X-ray diffraction data collected in oscillation mode. Methods Enzymol. *276*, 307–326.

Otwinowski, Z., Borek, D., Majewski, W., and Minor, W. (2003). Multiparametric scaling of diffraction intensities. Acta Crystallogr. A *59*, 228–234.

Prins, K.C., Cárdenas, W.B., and Basler, C.F. (2009). Ebola virus protein VP35 impairs the function of interferon regulatory factor-activating kinases IKKepsilon and TBK-1. J. Virol. *83*, 3069–3077.

Prins, K.C., Binning, J.M., Shabman, R.S., Leung, D.W., Amarasinghe, G.K., and Basler, C.F. (2010). Basic residues within the ebolavirus VP35 protein are required for its viral polymerase cofactor function. J. Virol. *84*, 10581–10591.

Reid, S.P., Cárdenas, W.B., and Basler, C.F. (2005). Homo-oligomerization facilitates the interferon-antagonist activity of the ebolavirus VP35 protein. Virology *341*, 179–189.

Sanchez, A., and Kiley, M.P. (1987). Identification and analysis of Ebola virus messenger RNA. Virology *157*, 414–420.

Sanchez, A., Kiley, M.P., Holloway, B.P., and Auperin, D.D. (1993). Sequence analysis of the Ebola virus genome: organization, genetic elements, and comparison with the genome of Marburg virus. Virus Res. *29*, 215–240.

Sanchez, A., Geisbert, T.W., and Feldmann, H. (2006). Filoviridae:Marburg and Ebola Viruses. In Fields Virology, D.M. Knipe, P.M. Howley, R.A. Griffin, M.A. Martin, B. Roizman, and S.E. Straus, eds. (Lippincott Williams & Wilkins), pp. 1409–1448.

Sanchez, A., Wagoner, K.E., and Rollin, P.E. (2007). Sequence-based human leukocyte antigen-B typing of patients infected with Ebola virus in Uganda in 2000: identification of alleles associated with fatal and nonfatal disease outcomes. J. Infect. Dis. *196* (*2*), S329–S336.

Schümann, M., Gantke, T., and Mühlberger, E. (2009). Ebola virus VP35 antagonizes PKR activity through its C-terminal interferon inhibitory domain. J. Virol. *83*, 8993–8997.

Shabman, R.S., Jabado, O.J., Mire, C.E., Stockwell, T.B., Edwards, M., Mahajan, M., Geisbert, T.W., and Basler, C.F. (2014). Deep sequencing identifies noncanonical editing of Ebola and Marburg virus RNAs in infected cells. MBio *5*, e02011.

Sheldrick, G.M. (2008). A short history of SHELX. Acta Crystallogr. A *64*, 112–122.

Shi, W., Huang, Y., Sutton-Smith, M., Tissot, B., Panico, M., Morris, H.R., Dell, A., Haslam, S.M., Boyington, J., Graham, B.S., et al. (2008). A filovirus-unique region of Ebola virus nucleoprotein confers aberrant migration and mediates its incorporation into virions. J. Virol. *82*, 6190–6199.

Tang, G., Peng, L., Baldwin, P.R., Mann, D.S., Jiang, W., Rees, I., and Ludtke, S.J. (2007). EMAN2: an extensible image processing suite for electron microscopy. J. Struct. Biol. *157*, 38–46.

Terwilliger, T.C. (2003). SOLVE and RESOLVE: automated structure solution and density modification. Methods Enzymol. *374*, 22–37.

Terwilliger, T. (2004). SOLVE and RESOLVE: automated structure solution, density modification and model building. J. Synchrotron Radiat. *11*, 49–52.

Thompson, J.D., Gibson, T.J., and Higgins, D.G. (2002). Multiple sequence alignment using ClustalW and ClustalX. Curr. Protoc. Bioinformatics *Chapter 2*, 3.

Trunschke, M., Conrad, D., Enterlein, S., Olejnik, J., Brauburger, K., and Mühlberger, E. (2013). The L-VP35 and L-L interaction domains reside in the amino terminus of the Ebola virus L protein and are potential targets for antivirals. Virology *441*, 135–145.

Watanabe, S., Noda, T., and Kawaoka, Y. (2006). Functional mapping of the nucleoprotein of Ebola virus. J. Virol. *80*, 3743–3751.

Winn, M.D., Murshudov, G.N., and Papiz, M.Z. (2003). Macromolecular TLS refinement in REFMAC at moderate resolutions. Methods Enzymol. *374*, 300–321.

Yabukarski, F., Lawrence, P., Tarbouriech, N., Bourhis, J.M., Delaforge, E., Jensen, M.R., Ruigrok, R.W., Blackledge, M., Volchkov, V., and Jamin, M. (2014). Structure of Nipah virus unassembled nucleoprotein in complex with its viral chaperone. Nat. Struct. Mol. Biol. *21*, 754–759.